



# Cycle ageing analysis of a LiFePO<sub>4</sub>/graphite cell with dynamic model validations: Towards realistic lifetime predictions



E. Sarasketa-Zabala<sup>\*</sup>, I. Gandiaga, E. Martinez-Laserna, L.M. Rodriguez-Martinez, I. Villarreal

*IK4-Ikerlan, Energy Business Unit, Arabako Teknologi Parkea, Juan de La Cierva 1, E-01510 Miñao, Spain*

## HIGHLIGHTS

- Methodology for cycle ageing semi-empirical model dynamic validation.
- Ageing tests acceleration evaluation.
- Detailed analysis of the influence of DOD, C-rate and Ah-throughput on cell ageing.

## ARTICLE INFO

### Article history:

Received 24 July 2014

Received in revised form

15 October 2014

Accepted 22 October 2014

Available online 29 October 2014

### Keywords:

Li-ion battery ageing

LiFePO<sub>4</sub> (LFP)/graphite

Cycle-life performance model

Dynamic cycling profiles

Lithium inventory loss (LLI)

Loss of active material (LAM)

## ABSTRACT

The present investigation work compares cycling ageing behaviour upon constant operation conditions (static tests) with degradation under non-constant schemes (dynamic tests), through a novel methodology for ageing model dynamic validation. A LFP-based Li-ion cell performance loss is analysed using a DOD and C-rate stress factors Ah-throughput-domain characterisation method, and represented using a semi-empirical model. The proposed stepwise validation approach enables assessing the static ageing tests acceleration factor and systematically improving the ageing model. The result is a simple but comprehensive model. The predictions root-mean-square error, under dynamic cycling operation conditions, is just 1.75%.

© 2014 Elsevier B.V. All rights reserved.

## 1. Introduction

Lithium-ion (Li-ion) batteries (LIB) are used in many commercial applications that require energy storage system (ESS) solutions. For large scale applications, which require not only high power and energy density but also long useful lifetime and safety guarantee, ageing analysis at cell level is one of the key issues for enhancing the integration of this technology. Unfortunately, internal resistance rise and capacity fade of Li-ion batteries over calendar and cycle life are still a major barrier for novel stationary and transport applications. Automotive and main stationary applications require 10–20 years of calendar life [1], which is still beyond the actual life of available LIB. It is therefore necessary to study in detail this

technology calendar and cycle ageing processes and their causes for understanding capacity and power fade over time.

Cell ageing in the course of time represents an important factor, but the properties of batteries also change with conditions of use. There are some applications that require high cycling capability of batteries. For instance, in automotive applications, while a personal car spends about 90–95% of its lifetime in storage mode when parked [2,3], heavy-duty hybrid electric vehicles (HEVs), such as buses and distribution trucks, generally are used between ten and fifteen hours per day all year around with high power demands in duty cycles [4,5]. The challenges are to find a way to cycle the battery system under optimal conditions and at the same time save as much fuel as possible. There are also stationary applications in which the battery would be mainly cycling over time, such as the grid system applications for transmission voltage support and frequency regulation.

There are numerous worldwide activities in the field of battery ageing analysis, modelling and lifetime prediction, which are

<sup>\*</sup> Corresponding author.

E-mail address: [esarasketa@ikerlan.es](mailto:esarasketa@ikerlan.es) (E. Sarasketa-Zabala).

approached from a wide range of perspectives. Cycling ageing studies are several [6–79] for different LIB technologies based mainly on: NCM (LiNiMnCoO<sub>2</sub>), LMO (LiMn<sub>2</sub>O<sub>4</sub>), NCM-LMO, NMO (Li(NiMn)<sub>2</sub>O<sub>4</sub>), LFP (LiFePO<sub>4</sub>), LCO (LiCoO<sub>2</sub>), LNCO (LiNiCoO<sub>2</sub>) and NCA (LiNiCoAlO<sub>2</sub>) with graphite as anode; and NCM/LTO (Li<sub>4</sub>Ti<sub>5</sub>O<sub>12</sub>, lithium titanate anode). Table 1 shows a literature review of main cycling ageing analysis on several Li-ion battery technologies (physical approaches are out of scope and this survey is focused on commercial and prototype batteries). This summary table reflects that indeed, there are many independent cycle ageing analyses. Some of them cover basic model electrical and electrochemical parameters, others aim at ageing modelling, and many of them are focused on post-mortem analysis for several chemistries. However, most of these analyses are based on performing ageing tests under either static conditions or under specific end-user profiles. Some authors analysed cycle life under specific dynamic application conditions and most of them were focused on vehicle operation [14,23,27,33,34]. S. Peterson *et al.* [34] evaluated differences between dynamic discharge (representing the driving) and constant discharge (energy arbitrage) using statistical analyses. T.M. Bandhauer *et al.* [80] also checked dynamic power profiles apart from constant current tests, but aiming at analysing thermal behaviour. So far, most of the ageing model validations are just based on either static impact factors evaluation [81,82] or specific application profiles evaluation [33,68]. The flexibility and/or accuracy of the built models for other conditions is scarcely evaluated. Therefore, there is a demand for the development of models that enable evaluating the degradation under different non-constant stress levels operating conditions [3,81,83]. It is crucial to develop models that progressively can be extended to other conditions and applications in a reliable way.

After reviewing the state of the art, it has been intended to develop a cell ageing predictive tool that can be implemented in different real applications. A methodology for lifetime prognosis has been developed, which comprises both cycle and calendar ageing but also their interaction in depth analysis. The main overall objective of this work includes the development of validation procedures for both ageing types models and the analysis of the applicability of the methodology [84]. The validation process not only consists of additional tests under other constant operating conditions (static validation) but also under non-constant impact factors operating schemes (dynamic validation). Aiming at the implementation of the systematic lifetime prognosis approach that was developed, the ageing behaviour of a commercial LFP/graphite 26650-type cell with 2.3 Ah nominal capacity was analysed. The LFP cathode has been considered as a promising candidate for Li-ion large scale applications because of its excellent chemical and

thermal stability, meaning safe performance, low cost, high specific power and high cycling capability [85–93]. Calendar ageing analysis of the selected reference was already described in Ref. [94]. The present paper focuses specifically on the analysis of cycling performance and the development of a thoroughly validated semi-empirical cycle ageing predictive model, as a further step towards an overall lifetime prognosis. Cycle ageing was studied as a function of depth of discharge (DOD), current rate (C-rate) and Ah-throughput (the amount of charge received and delivered by the battery). LFP-based large size LIBs cycling ageing studies are various in the literature [8,19,24,33,34,36,42,44,57,58,66,69,72], but this one enhances the results by adding further steps of dynamic validation that do not focus on testing specific end-user profiles. Some of the LFP cells ageing studies took into account both calendar and cycling ageing [57,66,69,72]. The present cycling work will be combined with the corresponding calendar ageing analysis [94] to provide an overall lifetime prognosis methodology. This methodology, which will be published elsewhere, is developed taking as priorities cost-effective solutions with minimum testing time and easy integration of measured parameters into the diagnosis tools for the applications.

## 2. Experimental

Single-factorial variation experiments were carried out using LFP/graphite 26650-type cells of the same manufacturing batch with 2.3 Ah nominal capacity and 3.3 V nominal voltage. For each cycling test a single cell was used in most cases, since:

- The cells reproducibility assessment at the Beginning of Life (BOL) using 74 cells indicated that the true population mean nominal capacity falls within  $2.313 \pm 0.005$  Ah range with 95% certainty.
- In a previous useful lifetime screening test using 3 cells per condition of the same reference, it was measured that the average coefficient of variation (CV) was just 6% over 2485 Full Equivalent Cycles (FEC, *i.e.* the number of complete (100% DOD) cycles corresponding to the total amount, charged and discharged, of Ah-throughput) under a charge-sustaining profile that included different highly demanding C-rates, both during discharge (9.7 and 6.5C) and charge (3.2, 4 and 2.9C).

Specific tests were however repeated in order to check the reliability of results. Range limits for the actively tested external influence factors were chosen within the cell operation window set by the manufacturer and taking also into account the cell behaviour observed during several initial screening tests. Nonetheless, C-rate outer limits were not checked since a real-life application may not operate in such conditions.

The ageing tests were performed in a temperature-controlled environment. CTS (Clima-Temperatur-Systeme, CTS/T-40/200/Li and CTS/T-40/600/Li models) and Prebatem Selecta (80 and 150 L chambers with Peltier effect) climatic chambers were used for this purpose. Both cycling and periodical check-up experiments were carried out using DIGATRON MCT (Multiple Cell Tester, MCT 100-06-10 ME and MCT 50-06-24 ME models) with BTS-600 data acquisition software.

### 2.1. Experimental procedures

Fig. 1 shows the flow chart for the testing procedure including both State of Health (SOH) controlling steps and accelerated cycle ageing tests. The latter (boxes in blue) are described in Section 2.2. Both capacity loss and internal resistance increase were measured in order to evaluate cell SOH over time and parameterise battery

**Table 1**  
Overall cycling lifetime prediction worldwide activity for most common chemistries used in commercial and prototype Li-ion cells.

Type of analysis	Reference
Cell characterisation studies with in situ electrical and/or electrochemical characterisation	[6–69]
Post-mortem analysis for identification of ageing mechanisms	[8,10,11,15,16,25,29,39,46,48,54,66,67,69–76]
- Analysis of impact factors effect (C-rate, DOD, T, SOC, etc.) under static conditions or specific end-user profiles	[7–9,14,17,19,24,26,30,31,33,51,57,61,65,74,77–79]
- Analysis of ageing mechanisms via in situ electrochemical characterisation	
Others:	
- Financial costs of different types of cycling	[34]
- Methodology for factors coupling	[36]

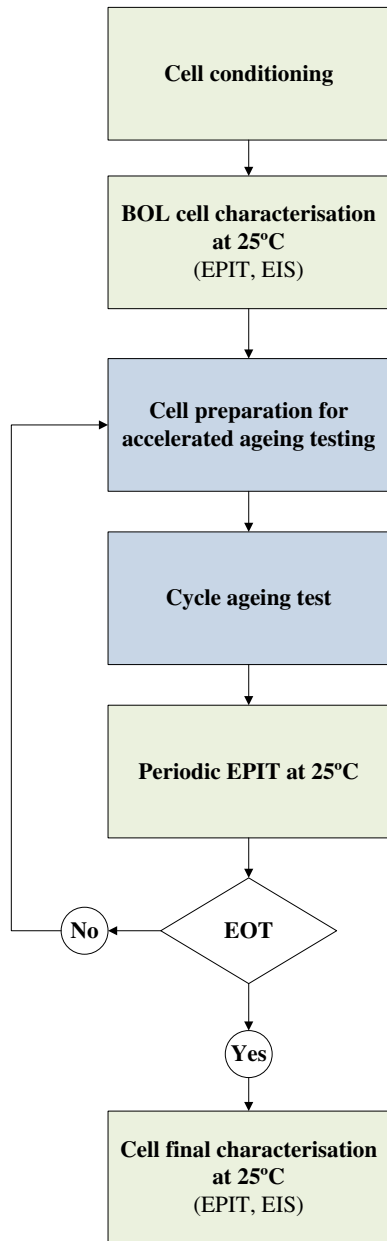


Fig. 1. Testing procedure used for ageing tests.

ageing model. Intermittent Electrical Parameters Identification Tests (EPIT), were carefully planned so that their impact on cell degradation was as negligible as possible. These tests were carried out at room temperature (25 °C) as follows:

- **Actual nominal capacity ( $Q$ ) measurement:** charge–discharge cycles (constant current–constant voltage, CC–CV, and CC modes, respectively) at nominal conditions specified by cell manufacturer (1C in CC mode). Three full charge–discharge cycles were performed in order to assess both reversible and irreversible capacity losses and check the repeatability of the results.
- **Close to equilibrium Open Circuit Voltage (quasi-OCV) measurements:** cell full discharge at C/5 C-rate (previous to discharge cells were charged in CC–CV mode at 1C). This C-rate was chosen as it was the largest one that enabled observing the voltage plateaus of the cell. Galvanostatic voltage profiles were used for examining electrode phase changes and understanding degradation phenomena.

- **Actual Direct Current (DC) IR measurement (Hybrid Pulse Power Test, HPPT):** 17 s current pulses at cell maximum acceptable charge and discharge C-rates (4C and 10C, respectively) over cell 90–20% SOC range with 10%  $\Delta$ SOC discharge intervals. After discharging the cells to specific SOCs, it was wait for 2 h before measuring the pulses. Regen and discharge pulses were measured one after the other at the same SOC level with 5 min rest period between pulses.

The first step, i.e. cell conditioning, consisted of formation–reactivation cycles carried out following the same procedure as for the nominal capacity test. Additionally, both BOL and cell further characterisation tests at End of Test (EOT) included *EIS measurements*, that consisted in impedance change evaluation in galvanostatic mode using frequency range from 0.1 Hz to 6.5 kHz at 25 °C at 30% and 70% cell SOC. This test was also occasionally included in EPIT.

## 2.2. Accelerated ageing tests conditions

### 2.2.1. Cycle ageing and static validation tests

Cycling ageing was initially investigated at several but constant DOD and C-rate cell operating conditions over time on the same cell. Different ageing processes were analysed in one by one experiments (single factorial experiments). Furthermore, C-rate and DOD binary combinations were analysed at certain chosen levels. Table 2 shows the cycling static accelerated ageing tests matrix. Ten different conditions were used for cycling ageing model development and an additional one at 2C and 100% DOD for the static validation (shaded in Table 2). Symmetric charge sustaining cycling performance was analysed. All the cycling tests were performed at 30 °C and 50% middle SOC (baseline temperature and voltage cycling conditions), and at CC charging–discharging mode. Fig. 2 shows the different cycling tests conditions, i.e. middle SOC and DOD ranges, in the quasi-OCV curve of the investigated cell (obtained from quasi-OCV test), illustrating the transformation processes the active materials performed over cycling. Different equilibrium phases of the cell system (single voltage plateau of the LFP electrode is coupled with the different transformation processes of graphite anode) are numbered (1–5) in the same Fig. 2. Experiments were carried out correcting set parameters values (SOC and DOD) according to cell actual nominal capacity ( $Q$ ). In case the cells were tested using always the same values of the impact factors, additional polarisation effects could show up in the data.

### 2.2.2. Dynamic validation cycling tests

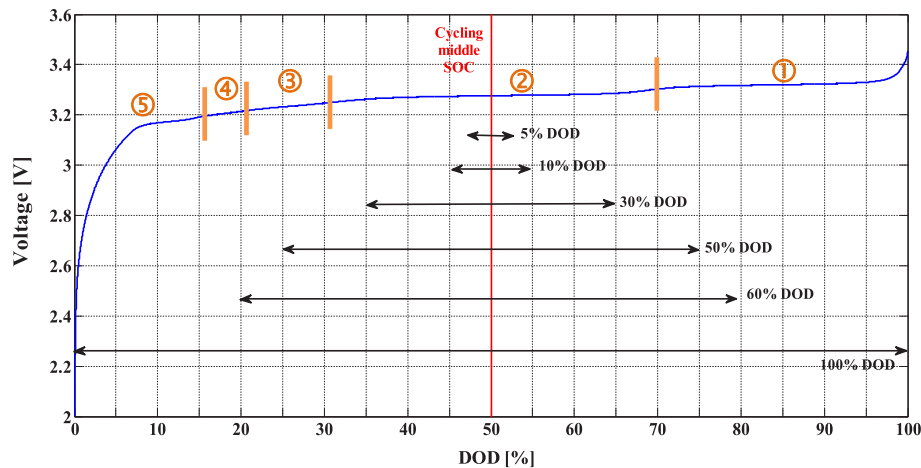
Additional tests under variable DOD and C-rate were carried out aiming at the validation of the cycling ageing model under different stress levels operating conditions. Two dynamic impact factors operation schemes that are plotted in Fig. 3 were planned. Both DOD (in red) and C-rate (in blue) were changed in each of the tests.

Table 2

Test matrix for cycling ageing analysis and modelling (static validation highlighted in grey). All the tests were done at 30 °C and 50% middle SOC.

C-rate	DOD [%]					
	5	10	30	50	60	100 <sup>a</sup>
1C	X	X	X	X	X	X
2C		X			X	X
3.5C		X			X	

<sup>a</sup> Cells were cycled between charge and discharge cut-off voltages (3.6–2 V), which corresponds with 97% DOD.



**Fig. 2.** Quasi-OCV curve of the studied 2.3 Ah LFP/graphite 22650-type cell. Graphite staging phenomena coupled with LFP voltage plateau numbered as 1 to 5. Cycling ageing testing conditions, middle SOC and DOD, are depicted in the graph.

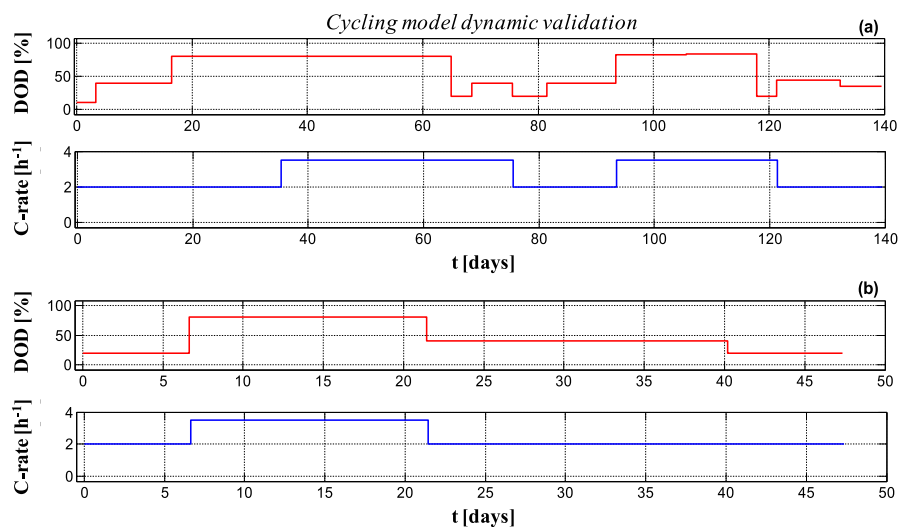


**Fig. 3.** Cycling ageing model dynamic validation. Two tests (a and b) under dynamic both DOD and C-rate over time at 30 °C and 50% middle SOC were performed.

### 3. Results and discussions

The effect of DOD and C-rate parameters upon cycling is discussed in the following section. Cell cycling behaviour is interpreted by combining different EPIT results. The cycle lifetime predictive model has been developed by introducing a comprehensive dynamic validation approach.

#### 3.1. Cell cycling performance fade evaluation

##### 3.1.1. Analysis of ageing results

The measured average nominal capacity of all the cells used under cycling examination was  $2.304 \pm 0.009$  Ah (95% CI) at the BOL. The evolution of cell performance ageing metrics (nominal capacity and internal resistance) when cycled at different DOD conditions are presented in Fig. 4 as a function of FEC. The evolution of DC internal resistance change during discharge at 50% SOC is just used for evaluating cell power performance fade due to cycling. As shown in Ref. [84] for a couple of tests as examples, the trend of measured internal resistance was similar despite the current pulse testing reference SOC and charge or discharge current step during

the check-ups. The comparison of capacity fade (Fig. 4(a)) and DC internal resistance increase (Fig. 4(b)) at a same DOD cycling condition shows that the cells under cycling lost significantly more capacity than power, alike under cell storage [94]. In addition, an unexpected slight initial decrease of IR was observed, in agreement with other studies with similar cells [57,79]. The moderate increase of total resistance (less than 10%) suggests that bulk transport properties are almost unchanged over cycling (absence of structural degradation) [95].

The shape of the nominal capacity loss curves in Fig. 4(a) indicates that the capacity loss trend changed upon cycling for 5% DOD and especially for 100% DOD tests, as illustrated in Fig. 5. Ageing behaviour was no longer linear but parabolic, as is typical for Li-ion technology according to the literature [96], after 2000–2500 FEC at 100% DOD. At the same time, the internal resistance increase tendency was also altered clearly following the same tendency (Fig. 5(a)), and especially between the last two EPIT. Cell failure after *ca.* 3000 FEC under 100% DOD cycling might be related to cell dry-out, *i.e.* loss of conductivity due to electrolyte consumption. For 5% DOD, the changes were not so marked (Fig. 5(b)), but both capacity loss and internal resistance increase

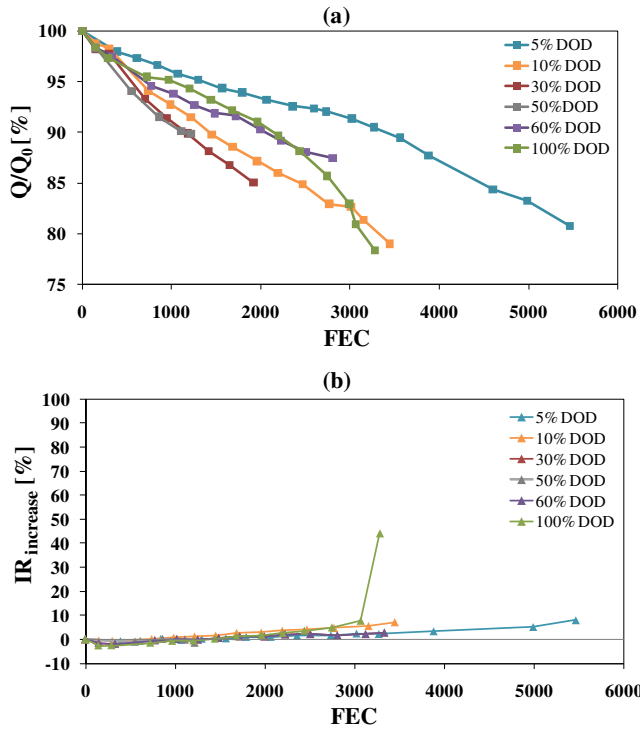


**Fig. 4.** (a) Actual nominal capacity ( $Q$ ) and (b) 17 s discharge DC internal resistance ( $IR$ ) increase, measured at 50% SOC, upon cycling (1C, 50% middle SOC and 30 °C) as a function of Full Equivalent Cycles (FEC), both normalised to initial nominal values ( $Q_0$ , initial nominal capacity).

rates changed after *ca.* 3000 FEC. Hence, it suggests that the dominant degradation mode is not the same over the whole cycle lifetime of the battery. The occurrence of the representative ageing effects changed upon ageing condition, so DOD effect was evaluated just considering the results before cell ageing process

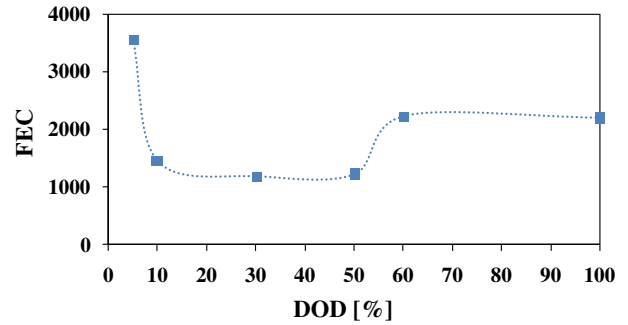


**Fig. 6.** Ranging of total number of Full Equivalent Cycles (FEC) that the cell could deliver at various DOD levels (1C, 50% middle SOC and 30 °C tests) before reaching *ca.* 90% SOH.

apparently changed (at *ca.* 90% SOH for the two cycling conditions where such change was observed). From data presented in Figs. 4 and 6 compares the total FEC that the studied cell could run under different DOD levels before the capacity drops to *ca.* 90% of the initial value (lifetime criterion where the ageing state for all the tests was similar). The presented Wöhler curve, which represents the cycling stress related to DOD against the total cycles up to the specified cell ageing state, is just bidimensional (at 25 °C, 1C and 50% middle SOC). It shows a non-linear dependency between FEC and cycle depth. Usually an exponential relationship is assumed, but the reference used in this work revealed that the cells cycled under large and small DODs both show the slowest degradation. Even though it is a rule of thumb that deep cycling considerably reduces the cycle lifetime of the battery due to the volume changes in materials (impact on the mechanical stability), experimental data shows that in this case 100% DOD level is not the most detrimental to the battery health (it was checked for a couple of cells, in which cell to cell variation was minimal). The cell FEC vs. DOD relationship does not show a single tendency either. Short cycles with low 5% DOD led to more than 3500 FEC. At 30% DOD level, the

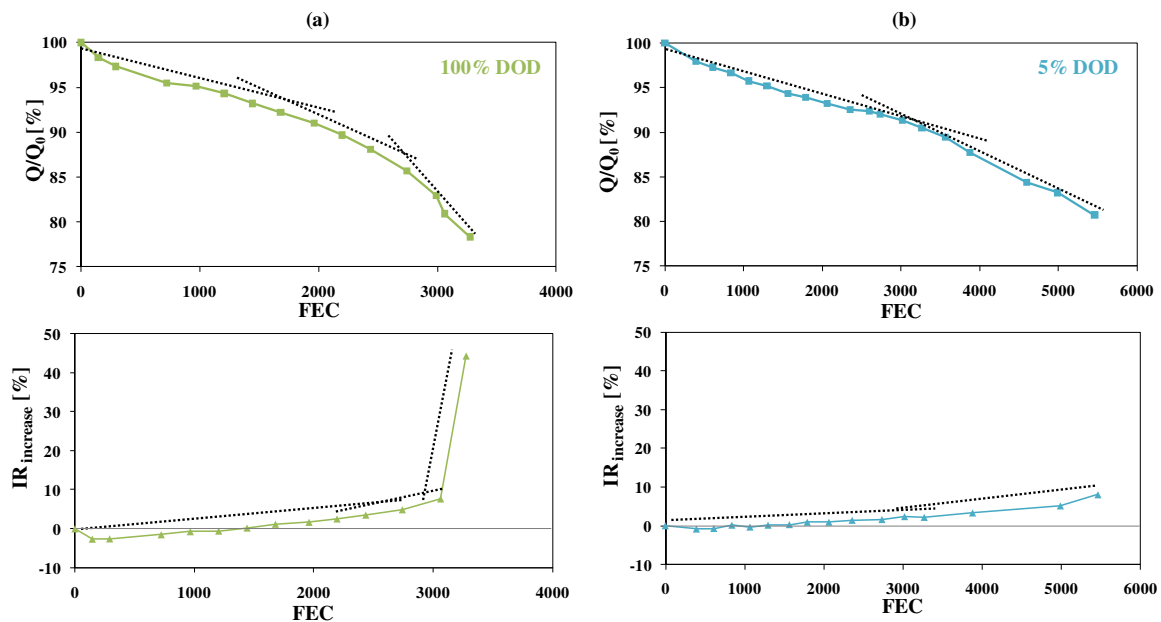


**Fig. 5.** Illustration of cells performance fade trends for (a) 100% DOD and (b) 5% DOD continuous cycling conditions (1C, 50% middle SOC and 30 °C). Actual nominal capacity ( $Q$ ) and 17 s discharge DC internal resistance ( $IR$ ) increase, measured at 50% SOC, as a function of Full Equivalent Cycles (FEC), both normalised to initial nominal values ( $Q_0$ : nominal capacity at the Beginning of Life).



least FEC were measured, but the number of cycles were similar in the 10–50% DOD range. According to the literature, phase changes in the battery materials during operation can lead to considerable mechanical stress [51,97] because the lattice parameters of materials change depending on predominant phases [98]. Fig. 2 shows the transformation processes that the studied active materials performed over cycling. At 10, 30 and 50% DOD cycling, the provided total FEC were similar (Fig. 6). However, Fig. 2 shows that the cells were cycled within the same voltage plateau of the graphite (2) in the case of 10 and 30% DOD and, at 50% DOD, there were over phase (1–3) changes. At 60 and 100% DOD the Ah-throughput was also similar (Fig. 6), slightly larger for the former, and in one case it was cycled over four different phases (1–4) and in the other over the five of them (Fig. 2). Hence, there is no clear relationship between cycling and graphite electrode staging phenomena for the studied commercial LFP/graphite cell. Figs. 2 and 6 show, contrary to M. Ecker *et al.* observations [51], that cells cycled in SOC ranges that crossed phase transitions of graphite electrode did not age faster, and that even for the same voltage plateau there is no correlation between ageing behaviour and DOD impact factor. Overall, the damage of cycle depth, staging phenomena itself and calendar ageing may all be superimposed. More data would be needed for deriving a direct correlation. Anyhow, there were demonstrated different DOD effect ranges, 10–50% DOD making a clear difference.

C-rate effect was also analysed. Fig. 7 shows the influence of DOD (a–c) and C-rate (d–f) parameters on cell capacity retention as

a function of FEC. When changing the cycling C-rate from 1C (Fig. 7(a)) to 2C (Fig. 7(b)), the capacity fade evolution was similar for 10 and 100% DOD levels. At these conditions (Fig. 7(d, f)), the influence of increasing the C-rate from 1 to 2C was negligible. At 60% DOD, even though capacity loss evolution was similar at different C-rates during the first 1000 FEC, the stress was afterwards enhanced at intermediate C-rate (2C). The cells cycled at 1C and 3.5C however, behaved similarly (Fig. 7(e)), but the capacity fade was even lower at 3.5C for a comparable number of FEC. This modification in the capacity retention tendency at 60% DOD revealed a change in the DOD effects comparison at 1C and 2C (Fig. 7(a, b)): while at 1C the performance fade was larger under 10% DOD than under 60% DOD, at 2C the results were similar regardless of the DOD. At 3.5C (Fig. 7(c)), again the capacity loss of the cell cycled at 60% DOD was lower than for the one at 10% DOD. At 10% DOD the degradation rate did not change remarkably with C-rate (Fig. 7(d)), although the larger the C-rate, the higher the capacity fade for this DOD level.

In conclusion, at large 100% DOD cycling, the amount of charge in the system overlaps the C-rate effect. The cycling time (calendar effect) induced the capacity loss more than the operating electric current, in agreement with the conclusions of E. Scott *et al.* [99] and also M. Ecker *et al.* [51], who found out that there is strong superposition of calendar ageing in high SOC range cycle depth. At low 10% DOD cycling, the effect of cycling time (or Ah-throughput) is more significant than C-rate, but there is also C-rate influence. At

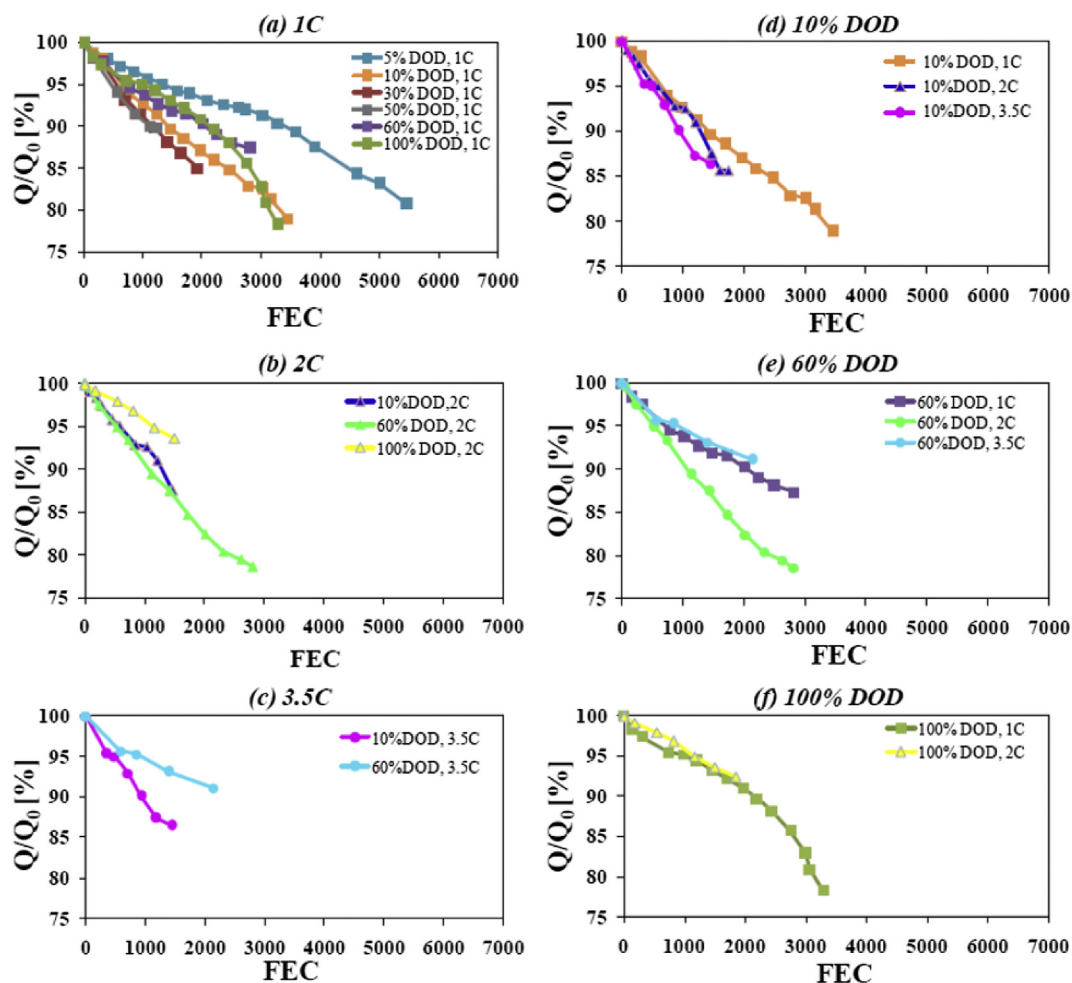
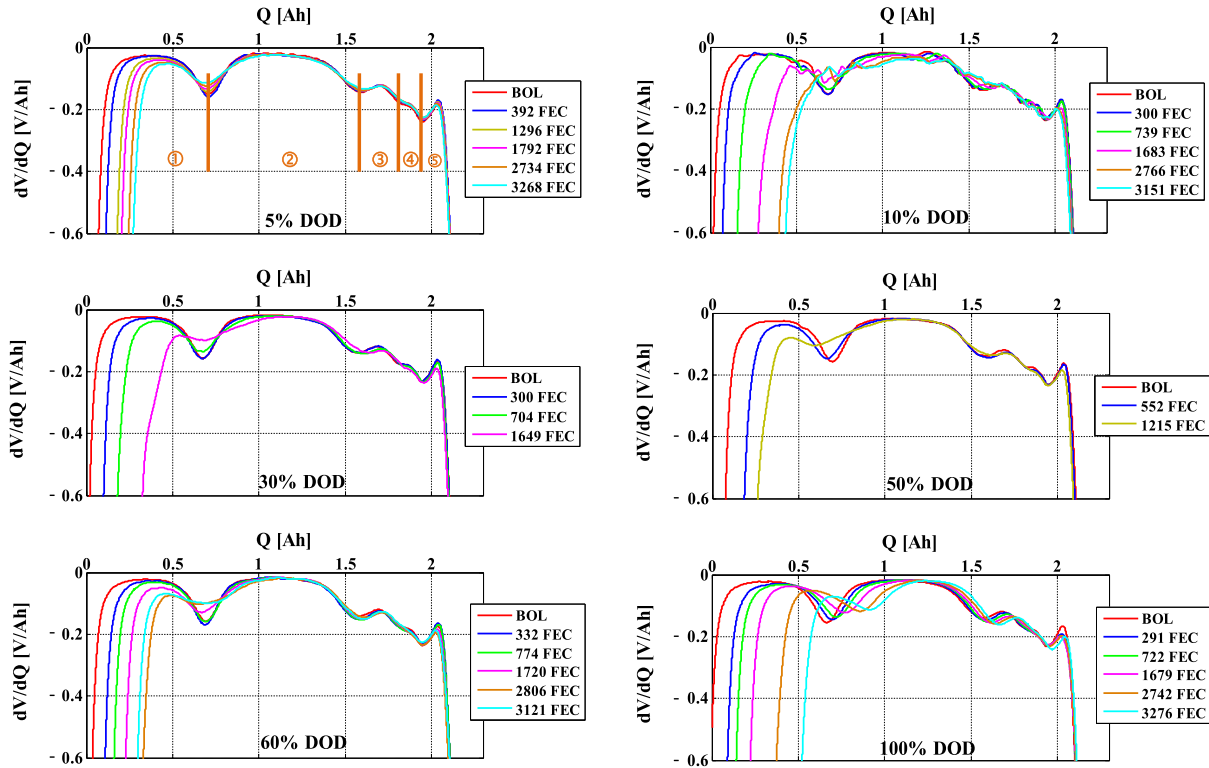


Fig. 7. Actual nominal capacity ( $Q$ ) normalised to initial nominal values ( $Q_0$ ) upon cycling (50% middle SOC and 30 °C) as a function of Full Equivalent Cycles (FEC). C-rate effect on capacity fade at different DOD (a–c) and DOD effect on capacity fade at different C-rate (d–f).



**Fig. 8.** Equivalent (same colour) and representative Differential Voltage (DV) curves, obtained from C/5 discharge voltage profiles, upon cycling at different DOD levels (1C, 50% middle SOC and 30 °C).

intermediate 60% DOD cycling, the effect of C-rate was enhanced but the trends are not in agreement with the general theory that the degradation rate increases with C-rate, as it was fulfilled for 10% DOD test. Contrary to expectations, ageing at this level was largely accelerated at the intermediate C-rate, 2C, and 3.5C cycling did not stand out. Hence, there are complex non-linear combined effects of DOD and C-rate, which additionally depend on DOD level (Fig. 6). More data would be necessary for an in depth interpretation of C-rate impact on cell degradation.

### 3.1.2. Analysis of cycling ageing mechanisms

The examination of close-to-equilibrium discharge curves (quasi-OCV EPIT, described in 2.1) using differential voltage (DV) and incremental capacity (IC) analysis ( $dV/dQ = f(V)$  and  $dQ/dV = f(Q)$ , respectively), provided insight into degradation phenomena. Fig. 8 presents DV curves for each cycling condition at different DODs. Numbering corresponds with voltage plateaus identified in Fig. 2. Equivalent FEC signatures are shown in the same colour and

only comparative data are shown (as EOT was not the same in all cases). The signatures for 10% DOD cycling condition indicated that there were measurement errors (test circuit issue at low C-rate), which hinder the identification of transitions from one electrochemically active phase to another.

The first valley shrank gradually in all cases, which demonstrates change of the stage 1 lithium-graphite compound [8] upon cycling. Hence, reduction of active lithium within the negative electrode at the beginning of cell discharge led to loss of lithium inventory (LLI). In the particular case of 100% DOD, all DV peaks but the last one moved towards larger SOC, which still requires analysis for further understanding. Barely any other changes were particularly highlighted from DV curves, but 5% DOD condition testing was extended up to ca. 5500 FEC, for which an analysis is not included in Fig. 8. Special attention was drawn to 5% DOD and 100% DOD due to observed ageing metrics tendencies changes (Fig. 5).

Fig. 9 shows more in detail the evolution of DV curves for 5% DOD cycling condition after prolonged operation, complementing

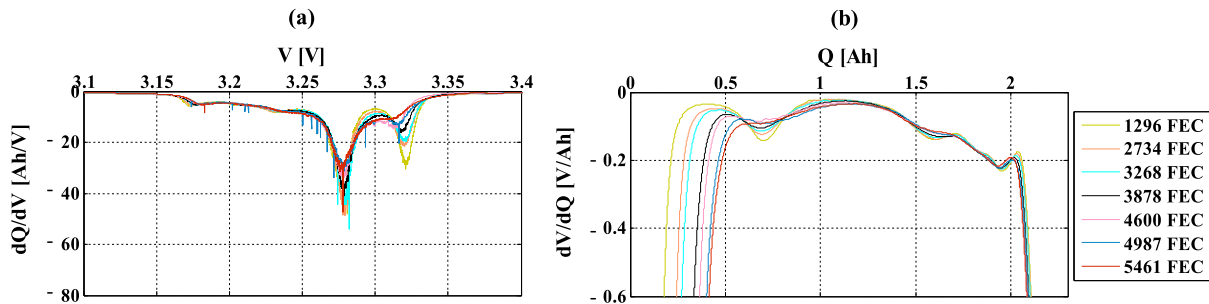


**Fig. 9.** (a) Incremental Capacity (IC) and (b) Differential Voltage (DV) curves, obtained from C/5 discharge voltage profiles, for 5% DOD test (1C, 50% middle SOC and 30 °C) upon cycling after large number of Full Equivalent Cycles (FEC).

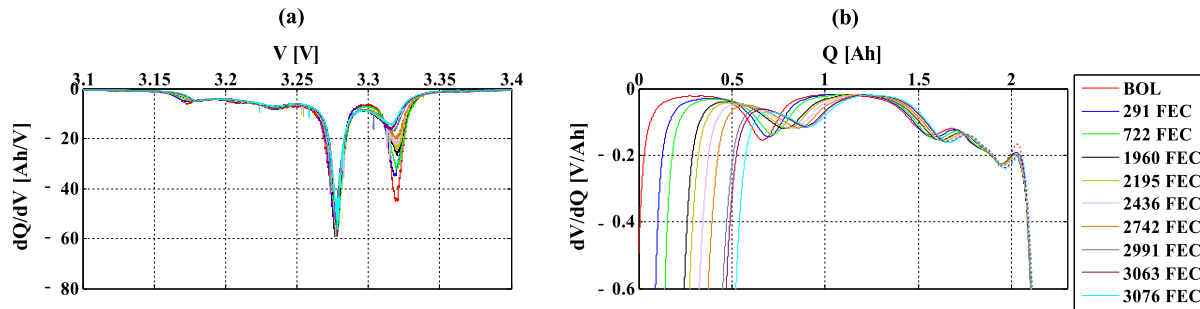


Fig. 10. Differential Voltage (DV) and Incremental Capacity (IC) curves, obtained from C/5 discharge voltage profiles, for 100% DOD test (1C and 30 °C) upon cycling.

the analysis with IC curves. In accordance with the ageing rate tendency change observed (Fig. 5), from 3068 FEC onwards peaks at low SOC (2–5 peaks) are also modified, even though the first peak did not disappear at all. Apart from the reduction of active lithium, graphite active material was apparently modified, and this electrode degradation showed up in different graphite staging processes (2–5 peaks intensities significantly reduced and peak 3–4 cannot be virtually distinguished). Hence, even though initially LLI was the main ageing phenomenon, the performance fade of the cell cycled at 5% DOD after prolonged cycling was apparently caused by a combination of LLI and LAM. From the signatures it is difficult to identify impedance changes, as all the IC peaks are notably modified, but its origin may be LLI.

Fig. 10 shows minutely (from 1679 FEC on) DV curves for 100% DOD cycling condition and also includes IC curves. In IC signatures (Fig. 10(a)) the peaks associated with the highest SOC (peak 1) are significantly more affected than the ones at lower SOC, indicating that LLI was apparently the main degradation mode. The size of the first peak reduced significantly upon cycling. This was also manifested in the respective first valley on DV curves (Fig. 10(b)), which corresponds with the reduction of the normalised capacity reduced in ca. 5.6% after 3063 FEC. Over the storage effect, mechanical stress during cycling might have enhanced the loss of exchangeable Li, which also apparently affected the electrode structure. All peaks/valleys in IC/DV curves somehow faded after prolonged cycling at 100% DOD, even though the first valley in DV curves (peak 1 in IC curves) was not completely lost. It was therefore concluded that LAM took place and assumed it to be related to active anode material alteration [100], which means that the graphite could not be lithiated to the same level as it was initially. All the transitions from one equilibrium to the other were affected (DV peaks shifting to larger SOC). The last DV peak barely shifted, with negligible changes in the last valley 5 (peak 5 in IC curves). The changes in the last valley 5 were negligible. None of the valleys disappeared at all, even though they changed gradually, so the graphite staging process could apparently be completed upon cycling. Regarding cell impedance changes, even though IC peaks were more or less positioned at the same voltages during nearly the entire cycling test, a shift towards lower voltages of the IC curve after 3063 FEC was detected, in agreement with the sharp DC internal resistance loss measured (Fig. 5 (b)). From IC and DC curves analysis, however, it was not possible to identify the effect responsible for the impedance change. For this reason, EIS spectra measurements were analysed.

Impedance change evolution for 100% DOD test, measured at 25 °C and 30% and 70% cell SOC, is shown in Fig. 11. Impedance measurements were carried out at different SOH for two different cells tested equally, which cell to cell variability upon cycling is shown in Fig. 12. Even though the resistance at medium frequency changed slightly at different EIS measuring SOC values (Fig. 11(a)

and (b)), it was considered not relevant. Previous work focused on the influence of SOC in DC internal resistance [84] corroborated this assumption. The high frequency intercepts with the real axis, which represents the resistance related to primarily the electrolyte (besides external leads and connections), is shifted to larger values indicating degradation of electrolyte. Conductivity of electrolyte seems to be therefore limited upon cycling, which is a result of organic deposition of the electrolyte on graphite surface (reduction of solvents proportion). This effect may have been enhanced due to high cell voltages (cycling was carried out between cell voltage limits). Higher SOC results in low anode potential, which causes electrochemical instability on electrolyte material [101].

Overall, at 5 and 100% DOD cycling conditions, the ageing processes phenomena was a combination of LLI due to progressive growth of SEI layer, LAM and cell impedance change. For the rest of the tests at different DODs, as for the EOT, the ageing state was still governed by LLI.

### 3.2. Cycle ageing predictive model

A semi-empirical cycle lifetime model was developed based on the following considerations in the previous section:

#### 1. Ageing metrics: capacity and internal resistance

The investigated LFP-based cell was primarily aged due to capacity fade rather than internal resistance increase. The cycle lifetime would therefore be limited by available capacity, as was the

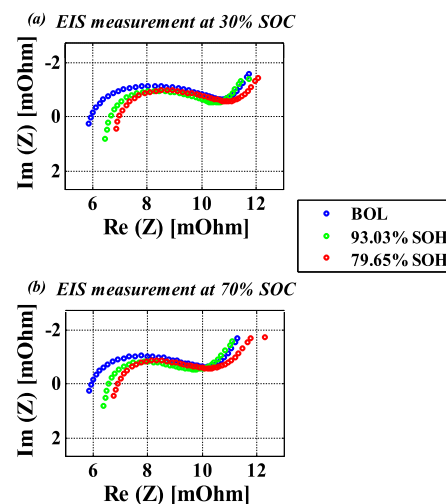
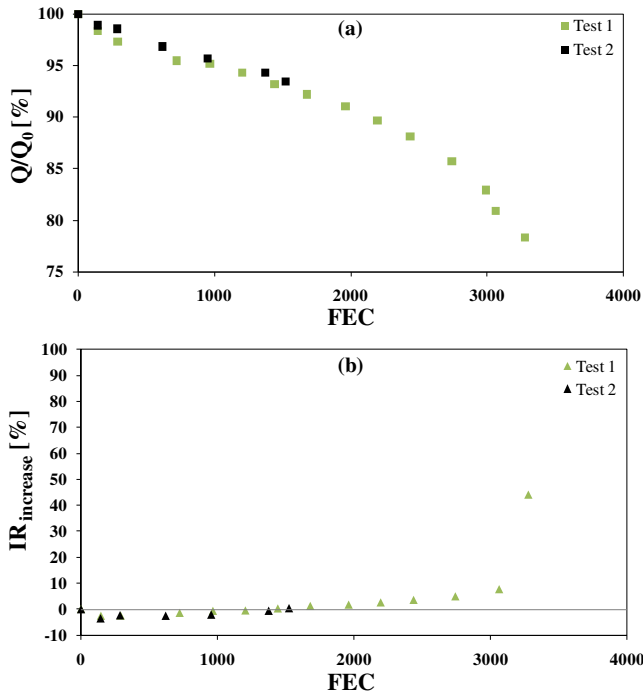


Fig. 11. Impedance spectra measured over different SOH (State of Health) at 25 °C and (a) 30% SOC and (b) 70% SOC, 100% DOD (1C and 30 °C) tests.





**Fig. 12.** Cycling at 100% DOD (1C, 50% middle SOC and 30 °C). (a) Actual nominal capacity ( $Q$ ) and (b) 17 s discharge DC internal resistance ( $IR$ ) increase, measured at 50% SOC, as a function of Full Equivalent Cycles (FEC), both normalised to initial nominal values ( $Q_0$  initial nominal capacity).

case for calendar lifetime [94]. This way, cycle ageing predictive model was focused on capacity loss evolution.

Instead of using time, Ah-throughput was chosen as a parameter for the cycle lifetime modelling.

## 2. C-rate and DOD effect

C-rate effect was minimal for some of the tests (Fig. 7) and it was different depending on DOD level. DOD and C-rate effects are combined at certain DOD levels. It would be therefore necessary to simulate the ageing trends due to C-rate for each cycling DOD. No tests were planned for such a study, as it is beyond the scope of this work (it requires to extend test matrixes for in detail evaluation). It is hence aimed at the step-wise implementation and validation of the proposed approach for lifetime prognosis (one of its goals is to minimise the experimental work). Hence, C-rate effect was not taken into account in the cycling ageing model.

The capacity fade fitting would then include data of the conditions in the text matrix at 1C (Table 2), containing six different conditions.

Within this framework for cycle ageing modelling, the test planned for the model static validation (2C and 100% DOD) could not be used with the initial purpose (C-rate effect was not modelled). On the other hand, no 1C test was set apart for the static validation, after considering all the data necessary for the modelling.

## 3. DOD and Ah-throughput effect

It was observed that the DOD and Ah-throughput relationship do not follow a single dependency (Fig. 6), i.e. that the DOD impact factor effect for the investigated cell is different depending on the DOD level. Hence, the DOD factor effect would be modelled in different ranges.

## 4. Ageing phenomena

It was confirmed that electrolyte degradation and SEI layer evolution dominates the cycle ageing (LLI), despite the occurrence of other consequential effects. LAM was detected but it was induced after different Ah-throughput depending on the ageing conditions. Hence, it was decided not to consider experimental data after the detected inflexion points (Fig. 5) that indicate transition to the combination of different ageing processes, as verified from close-to-equilibrium curves analysis (Figs. 9 and 10).

To determine the most appropriate mathematical functionalities that match the conclusions from ageing analysis and also to determine the fitting parameters rearranging the terms, a multistep optimisation process was implemented based on least square fitting method. As for the calendar ageing model [94], a single main degradation mode was modelled. Different steps also defined the best DOD ranges for the two equations used for capacity fade modelling. Eqs. (1) and (2) show the overall semi-empiric mathematical model for cycle ageing, where  $\alpha_3$ ,  $\beta_3$ ,  $\alpha_4$ ,  $\beta_4$ ,  $\gamma_1$ ,  $\gamma_2$  and  $\gamma_3$  are constant fitting parameters. Eq. (1) fits ageing data for 10–50% DOD range. Eq. (2) fits ageing data for the rest DOD levels and also adjusts to the transitions between the two identified DOD ranges, besides permitting extrapolations below 5% DOD (10% > DOD & DOD > 5%). The level of stress was increased due to the charge in the system (Ah-throughput), as for calendar ageing, square root of time capacity fade dependency was observed ( $t^{0.5}$ ) [94]. LLI was therefore enhanced due to the mechanical stress during cycling. The cycling performance loss as a function of Ah-throughput was, in addition, different depending on DOD level (Ah<sup>0.87</sup> or Ah<sup>0.65</sup>).

$$Q_{loss, cycling} [\%] \left( 10\% \geq DOD \geq 50\% \right) = \left( \gamma_1 \cdot DOD^2 + \gamma_2 \cdot DOD + \gamma_3 \right) \cdot Ah^{0.87} \quad (1)$$

$$Q_{loss, cycling} [\%] \left( DOD < 10\% \& DOD > 50\% \right) = \left( \alpha_3 \cdot \exp(\beta_3 \cdot DOD) + \alpha_4 \cdot \exp(\beta_4 \cdot DOD) \right) \cdot Ah^{0.65} \quad (2)$$

Fig. 13 shows the capacity loss experimental results at different DOD levels (solid markers) and the corresponding predictions (lines) using the developed model. Data not considered for the modelling, as mentioned above, are shadowed using the same colour as the experimental data solid markers (5% DOD and 100% DOD). For such cases, in case the EOL was not defined beforehand, the lifetime would be over-estimated and the ageing phenomena may lead to sudden fade. Goodness of capacity loss fit was

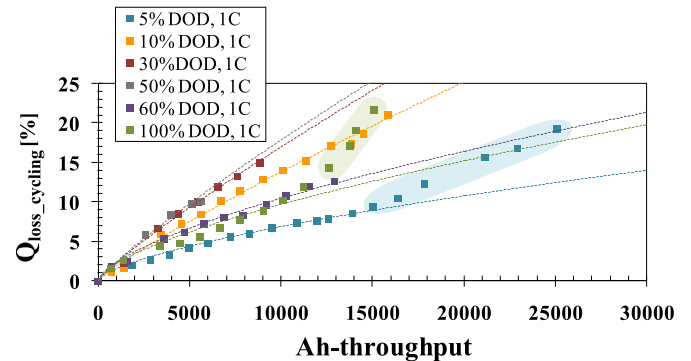


**Fig. 13.** Capacity loss ( $Q_{loss}$ ) data at different cycling DOD levels (solid colour markers) and fitted cycle ageing model (continuous lines) for cycling at 1C, 50% middle SOC and 30 °C.

evaluated for all experimental data at each cycling condition, except for data within shadowed areas (not considered for the fitting). Box plot in Fig. 14 shows the distribution of modelling residuals. The average values for each group of data are illustrated with open circles and the median with a line inside the boxes. There was one outlier in 30% DOD experimental data. The fitting accuracy was the highest for 5% DOD cycling condition: its residuals variance was just 0.01%, interquartile range 0.15% and median 0.12%. The largest difference between fitting and experimental data was for 100% DOD cycling condition, but the model results were still good. Whiskers showed 0.22% variance and the median was 0.47%, but the residuals showed symmetric distribution. 50% DOD fitting showed the largest median residual value (0.51%), but the sample size at this condition was not representative ( $N = 4$ ). The accuracy of the model for each fitted cycling condition (1C, 50% middle SOC and 30 °C) is ranged as follows: 5% > 30% > 60% > 10% > 50% > 100% DOD. All in all, the mean overall fitting residual was just 0.32% and 1.45% the maximum.

The suitability of the developed function for the cycle life model was further assessed against different operating C-rates. Eqs. (1) and (2) were used to fit capacity loss evolutions at each C-rate, as shown in Fig. 15. Prediction errors are evaluated in Fig. 16. The mean prediction error was 1.44%, for which major contribution was coming from 10% DOD and 3.5C cycling condition prediction. The source of the error was not therefore the change of the power law relation, as it changed especially under 60% DOD and 2C cycling condition, in agreement with the observations from Fig. 7.

#### • Dynamic validation

Additional tests were run in order to check model validity under more realistic cycling conditions that the model would have to face for predicting lifetime in real applications. These tests consisted of making dynamic upon cycling the controllable cycling ageing impact factors that were considered within this work, i.e. DOD and C-rate. The defined two dynamic validation tests profiles were shown in the experimental section. To evaluate the effect of the sequences in the same load collectives shown in Fig. 2, it was assumed, in agreement with H. Wenzl *et al.* [102], that the degradation caused by a new event is independent of the cell history (previous cycles) that induced accumulated ageing. Fig. 17 shows capacity loss experimental data (open markers) and the corresponding predictions using Eqs. (1) and (2) (dotted lines with the same colour as the corresponding experimental data markers). Results showing capacity recovery are encircled in red. In such

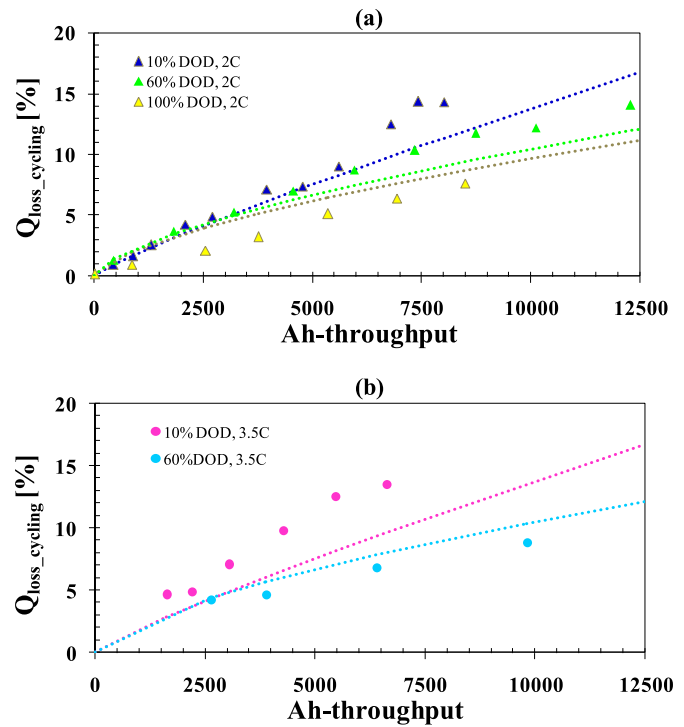


Fig. 15. Capacity loss experimental data (markers) and predictions (dotted lines) under cycling under different DOD conditions and C-rate conditions: (a) 2C and (b) 3.5C.

cases, the level of stress in the cell was reduced due to either the cycling conditions or pause times before and after the check-ups at some time. These data are set apart as the developed capacity loss model is accumulative upon ageing and would never be able to predict cell capacity rise because of reversible phenomena. The prediction methodology under dynamic cycling conditions takes into account the ageing by former usage, so the residual capacity is used as a reference point for further predictions at different operating parameters and not simply the operating time [102,103]. The total ageing time is the sum of the cycling time periods at different DOD and C-rate conditions. It appears that the general irreversible capacity offset trend is followed. However, it is difficult to describe the relationship between the mathematical correlation and measured cell performance loss, and even to qualitatively understand capacity fading behaviour for the different conditions upon cycling.

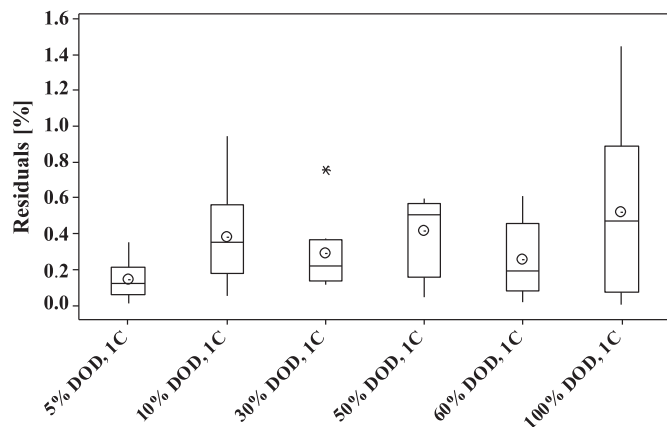


Fig. 14. Box plot of capacity fade prediction residuals distribution for each modelled cycling condition.

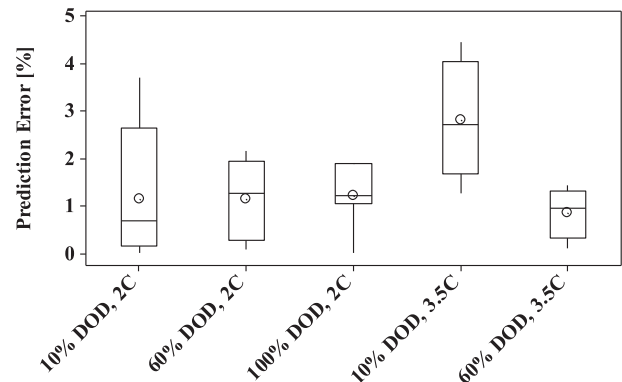
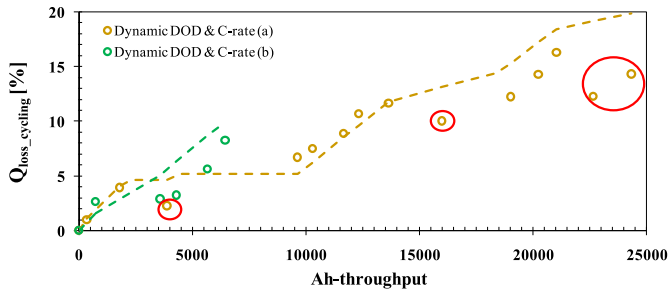


Fig. 16. Box plot of capacity loss prediction errors distribution for cycling conditions at C-rates different from modelled 1C condition.



**Fig. 17.** Capacity loss ( $Q_{loss}$ ) data (markers) under dynamic cycling conditions (Fig. 3 (a and b)) and corresponding simulation results (dotted lines). Cycling under dynamic, DOD and C-rate, 50% middle SOC and 30 °C.

### • Methodology for dynamic validation and improvement of the cycle ageing model

Initially, the two dynamic cycling tests presented were just planned (Fig. 3). Different both C-rate and DOD periods were combined at a time, as one of the targets of the lifetime prognosis methodology was to minimise the time consuming and cost-intensive experimental work. However, in view of the complexity of the results (Fig. 17), it was considered interesting to carry out additional tests and a methodology for cycling ageing dynamic validation was defined, which is outlined in the flow chart in Fig. 18. After the combined analysis of different cycle ageing impact factors under dynamic conditions (*Dynamic validation I*), in case it were necessary, the methodology would propose to also study individually DOD and C-rate parameters single effects more in depth under

non-constant profiles (*Dynamic validation II*). These analyses intend to provide insight into the combined effects analysis (*Dynamic validation I*). However, if believed necessary, more additional tests would be suggested (*Dynamic validation III*) for an in depth understanding of cell ageing behaviour under more realistic cycling operation conditions.

The first step (cycling at variable both C-rate and DOD) of the dynamic validation methodology was already fulfilled, with no clearly evaluable trends (Fig. 17). Further tests that were defined for the dynamic validation of individual DOD and C-rate impact factor effects (*cycling model dynamic validation II*), are shown in Fig. 19. Fig. 20 shows experimental results of the dynamic DOD and C-rate cycling tests (markers) and the corresponding predictions (dotted lines), using the cycling ageing model (Eqs. (1) and (2)) and the previously described methodology for predictions at non-static conditions. The cycle ageing predictions show that the total capacity loss according to the semi-empirical mathematical model is independent of any sequence of DOD (Fig. 19 (a,b) profiles simply change the order of the events). Experimental verification in Fig. 20 however indicates that there is a slight dependence on the sequences, although both DOD profiles (Fig. 19(a,b)) led roughly to the same overall degradation. At different C-rates, the differences do not attract so much attention either. Overall, from *cycling model dynamic validation II* it was concluded that cycle ageing depends little on the sequences of the cycles either DOD or C-rate, which confirms the hypothesis adopted for the modelling (degradation independent on cell history). However, it is necessary to verify the degradation that occurs when intercalating events of storage operation between cycling sequences.

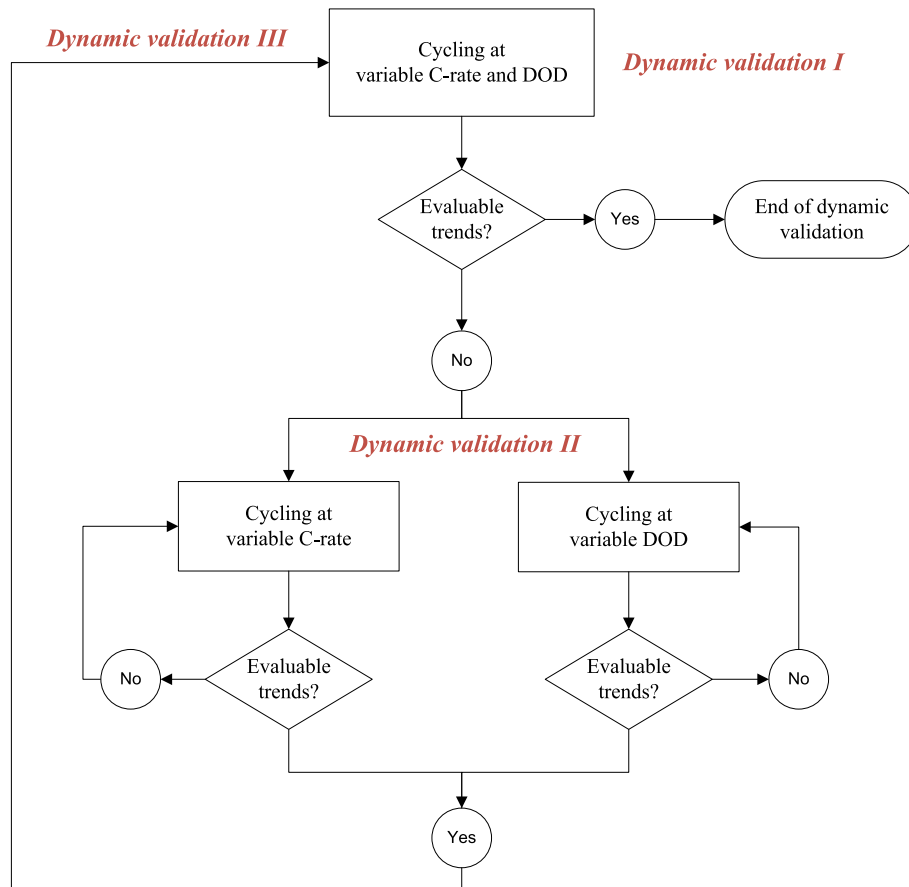


**Fig. 18.** Testing procedure for cycling ageing dynamic validation.

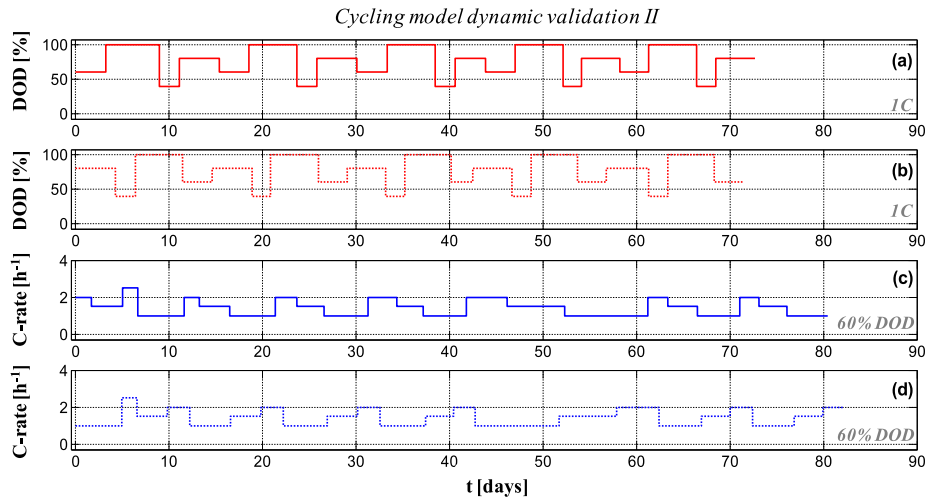


**Fig. 19.** Cycling ageing model dynamic validation II. Four different tests defined under dynamic either DOD (1C) or C-rate (60% DOD), 50% middle SOC and 30 °C. Two tests under dynamic DOD (a,b) and other two under dynamic C-rate (c,d).

Results from cycling the battery under dynamic power profile (Fig. 20(c,d)) also showed that the models based on constant-current data at just 1C predict the dynamic performance data well. It suggests that, for the cell reference studied in this paper, the effect of DOD on capacity fade was larger than that of the C-rate, under the specified conditions. Moreover, the prediction accuracy was improved under dynamic C-rate conditions, which verifies that the developed model adapts properly to dynamic battery behaviour. The mean prediction error was enhanced from 1.44% (under

static C-rate conditions) to 1.16% (under dynamic C-rate conditions). However, prediction accuracy diminished under dynamic DOD continuous cycling conditions (Fig. 20(a,b)). Capacity loss predictions were distinctly over measured data, but keeping the same tendency. It seemed that such over-estimation was controlled by a critical factor. This characteristic was revealed for estimations under dynamic DOD conditions and not for dynamic C-rates at a constant DOD. Moreover, after 4000 Ah-throughput the capacity loss under dynamic DOD conditions was in the range of 3–3.5%, whereas it was 4–8.5% under static DOD conditions (Fig. 13). Therefore, the initial conclusion was that the cell degradation is lessened under dynamic DOD conditions, which means that the ageing acceleration factor for different static DOD tests is larger than that for dynamic DOD tests. The ageing predictive model, which is a function of DOD and Ah-throughput, was developed based on static tests data, and this is apparently why it over-estimates the ageing under dynamic DOD conditions. Going back to the initial cycling model dynamic validation (Fig. 17), this conclusion could not be clearly demonstrated, as data did not show any marked tendency. Aiming at overcoming the discrepancies between modelling results and experimental data, additional tests under dynamic both C-rate and DOD operation schemes were carried out.

Aiming at a comprehensive cycle ageing model validation, Fig. 21 shows the defined test profiles for the *cycling model dynamic validation III* step. They covered DOD levels that were not evaluated in the modelling process (such as 20%, 40% and 80% DOD) and the C-rate was also made much more dynamic. This is an attempt to evaluate the C-rate issue under more exigent conditions, as evidenced in the profiles defined in Fig. 21(b). Fig. 22 presents these last C-rate and DOD dynamic validations experimental results (markers) and simulation outputs (dotted lines) based on Eq. (1), Eq. (2) and the prediction methodology that takes into account the accumulated ageing each time the operating parameters change. This closer examination of both cell ageing behaviour and the established cycle ageing model goodness demonstrated that:

- The impact of the C-rate factor is not large and its level of influence on capacity loss rate does not stand out (it is negligible).
- The developed model for 50% middle SOC and 30 °C, based on static and symmetric cycling conditions tests results, over-estimates the cell capacity fade under dynamic operation.

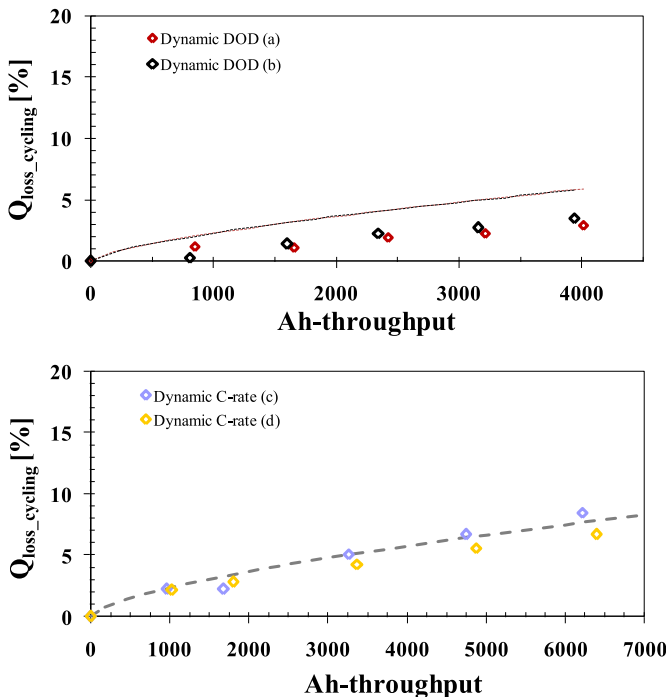


**Fig. 20.** Capacity loss ( $Q_{loss}$ ) data (markers) under: (a,b) dynamic DOD cycling conditions (Fig. 19 (a,b)) and corresponding simulation results (dotted lines). Cycling under 1C, 50% middle SOC, 30 °C and dynamic DOD; (c,d) dynamic C-rate cycling conditions (Fig. 19(c,d)) and corresponding simulation results (dotted lines). Fittings are super-imposed because the DOD is the same for both tests and the predictions do not include the C-rate effect. Cycling under 60% DOD, 50% middle SOC, 30 °C and dynamic C-rate.

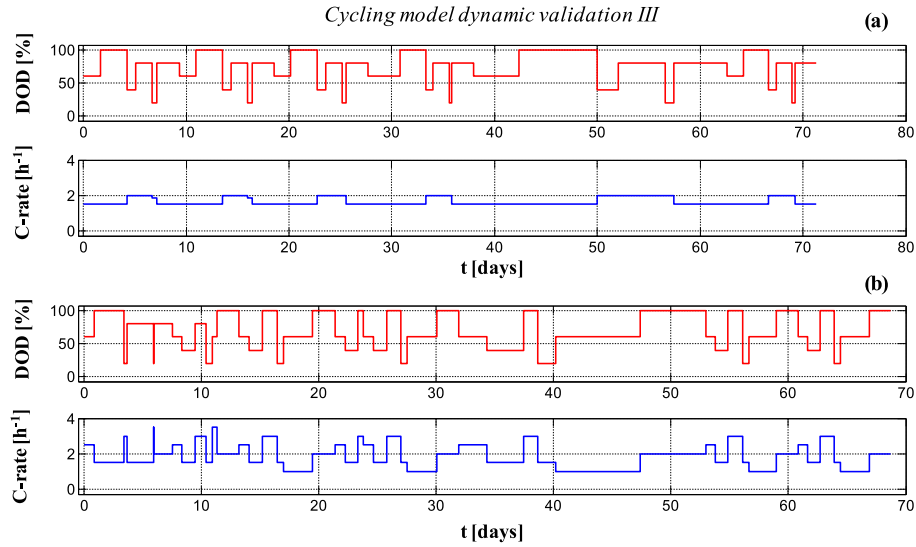


Fig. 21. Cycling ageing dynamic validation III. Additional two tests (a and b) under both dynamic DOD and C-rate over time at 30 °C and 50% middle SOC.

Continuous cycling at static conditions accelerates the cell ageing more than continuous cycling under dynamic conditions, although the latter tests were also accelerated. The acceleration factor for static ageing continuous conditions is mainly influenced by the DOD factor.

The solution for improving the reliability of the cycle ageing predictive model was to introduce a novel balancing factor that deals with the ageing acceleration issue. Aiming at a this factor modelling, the effect of DOD parameter on capacity loss under dynamic and static conditions was compared. The respond matrix was contrasted with observation data and the best complex factor coefficient, namely  $k$ , was assessed performing the prediction errors analysis.  $k$  acceleration factor was modelled as a function of Ah-throughput.

Fig. 23 shows the predictions using the cycle ageing model with the DOD ageing effect acceleration correction factor implemented for dynamic operation estimations, as indicated in Eqs. (3) and (4). The predictions root-mean-square error (RMSE) for dynamic DOD cycling improved from 2.20% (Fig. 20(a,b)) to 0.88% when implementing the ageing acceleration correction factor (Fig. 23(a)). It also improved consistently for the predictions of the four tests that

combined dynamic both C-rate and DOD events: from 2.79% RMSE (Figs. 17 and 22) to 1.75% RMSE (Fig. 23(b,c)).

$$Q_{\text{loss, cycling}} [\%] \quad (10\% \geq \text{DOD} \geq 50\%) \\ = (\gamma_1 \cdot \text{DOD}^2 + \gamma_2 \cdot \text{DOD} + \gamma_3) \cdot k \cdot \text{Ah}^{0.87} \quad (3)$$

where  $k = 1$  in case the DOD factor is constant over time

$$Q_{\text{loss, cycling}} [\%] \quad (\text{DOD} < 10\% \& \text{DOD} > 50\%) \\ = (\alpha_3 \cdot \exp(\beta_3 \cdot \text{DOD}) + \alpha_4 \cdot \exp(\beta_4 \cdot \text{DOD})) \cdot k \cdot \text{Ah}^{0.65} \quad (4)$$

where  $k = 1$  in case the DOD factor is constant over time

Overall, the presented semi-empirical model successfully represents the cycling behaviour of the cell both at static and dynamic cycling operation conditions at 30 °C and 50% middle SOC. This cycle ageing model will be combined with the calendar ageing model published in Ref. [94] for predicting the battery lifetime under other temperatures (30–50 °C) and middle SOC conditions, and also under charge depleting operation modes that include different C-rates and 10–90% SOC range. This novel joint prediction modelling approach will be published in detail elsewhere. Preliminary results indicate an excellent response to the complex operation of different realistic applications.

#### 4. Conclusions

Cycling dynamic validations provided many important results regarding C-rate and DOD effects under non-constant schemes for promoting the understanding of cycle ageing phenomena. Overall, eight cycling ageing model dynamic validation tests were carried out, which were defined with different specific goals for an extensive capacity loss evaluation. It was concluded that it should be started with a simple preliminary test that combines both C-rate and DOD impact factors, instead of carrying out a long-lasting validation test, for deciding whether it would be necessary an individual validation protocol for every single impact factor.

The presented semi-empirical cycle ageing model for a LFP-based cylindrical cell was developed after understanding ageing

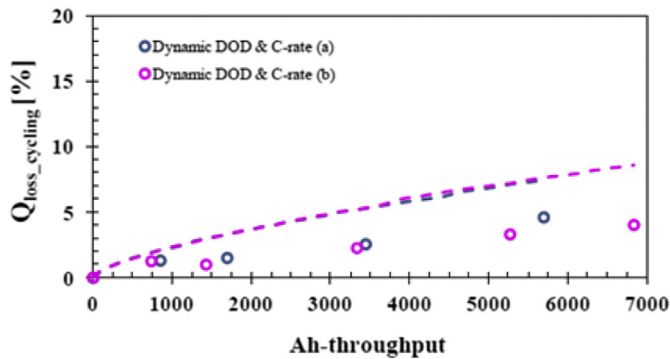
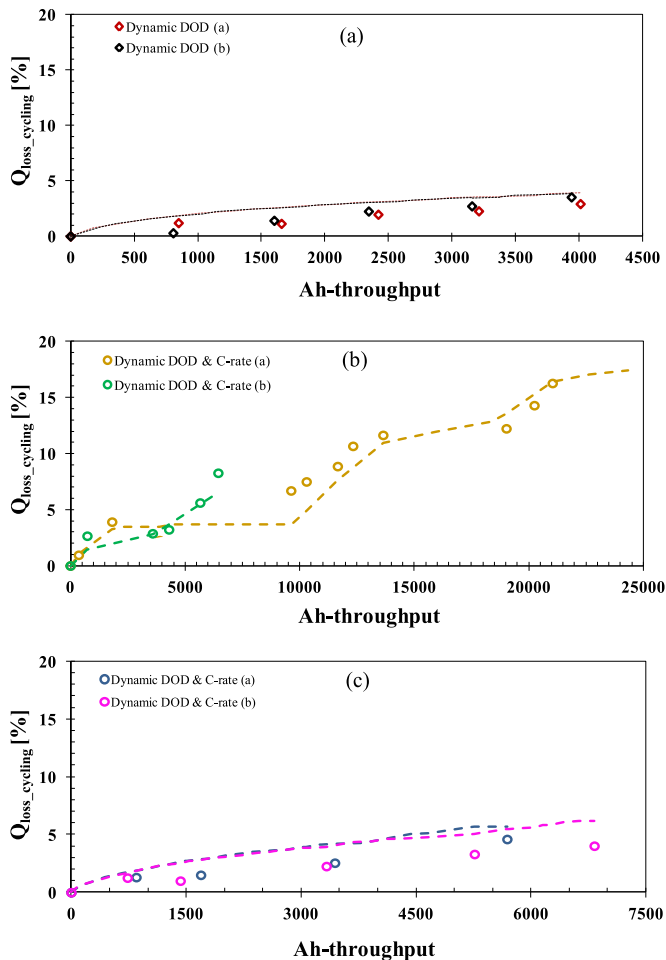


Fig. 22. Capacity loss ( $Q_{\text{loss}}$ ) data (markers) under dynamic cycling conditions (Fig. 21) and corresponding simulation results (dotted lines). Cycling under dynamic, DOD and C-rate, 50% middle SOC and 30 °C.





**Fig. 23.** Capacity loss ( $Q_{loss}$ ) data (markers) under: (a) dynamic DOD cycling conditions in Fig. 19(a,b) and the corresponding simulation results (dotted lines) using the static ageing acceleration factor  $k$ . Improvement of the prediction shown in (Fig. 20(a,b)); (b) dynamic DOD and C-rate cycling conditions in Fig. 3 and the corresponding simulation results (dotted lines) using the static ageing acceleration factor  $k$  (Eqs. (3) and (4)). Improvement of the predictions shown in Fig. 17; (c) dynamic DOD and C-rate cycling conditions in Fig. 21 and the corresponding simulation results (dotted lines) using the static ageing acceleration factor  $k$  (Eqs. (3) and (4)). Improvement of the predictions shown in Fig. 22.

phenomena under DOD and Ah-throughput impact factors. It is based on capacity loss and LLI main degradation mechanism, as the combined analysis of capacity and internal resistance ageing metrics, IC and DV curves and EIS spectra indicated. The developed model does not include C-rate factor, but it is able to predict precisely its effect as well. This is corroborated by applying the model prediction to different static C-rates operation conditions experiments not used for modelling. Even further tests at dynamic C-rate conditions show better agreement between experimental and model results, validating the proposed cycling model. In general, it cannot be assumed that the C-rate impact factor effect would not be relevant for another different reference. Hence, it is not a simplification that comes as a result of the methodology, but it was validated comprehensively by means of the dynamic validation of the developed model.

It was demonstrated that static cycling degrades the cell more than dynamic operation. That means that the prediction based on the static modes underestimates the lifetime. The initial proposed model systematically over-estimates capacity loss upon dynamic cycling conditions. Therefore, ageing acceleration rate was

modelled and this factor was introduced in the cycling model. Taking all this into account, more realistic cycle ageing predictions are feasible with just 1.75% RMSE.

The overall scope, where this work is included, is to develop a lifetime prognosis methodology that combines both calendar and cycle ageing effects and covers a wide range of operation conditions of different applications and systems. Therefore, further work to complete this development included non-symmetric cycling with discharge periods at up to ca. cell maximum C-rate (10C) and charge depleting complex profiles (e.g. combination of cycling, rest periods at different SOCs, incomplete charging, etc.) under different temperatures. The complete methodology and comprehensive validation results will be published elsewhere.

## Acknowledgement

This investigation work was financially supported by ETORTEK (Energigune'12 – I + D + i en almacenamiento de energía electroquímica y térmica, y en energía marina, IE12-335) and EMAITEK Strategic Programs of the Basque Government.

## References

- [1] D. Rastler, in: Electric Power Research Institute (EPRI), 2010.
- [2] A. Eddahech, O. Briat, E. Woigard, J.M. Vinassa, *Microelectron. Reliab.* 52 (2012) 2438–2442.
- [3] S. Grolleau, A. Delaille, H. Gualous, P. Gyan, R. Revel, J. Bernard, E. Redondo-Iglesias, J. Peter, *J. Power Sources* 255 (2014) 450–458.
- [4] B.Y. Liaw, M. Dubarry, *J. Power Sources* 174 (2007) 76–88.
- [5] E. Jobson, in: European Fleets Conference, Örebro, Sweden, 2010.
- [6] J. Wang, P. Liu, J. Hicks-Garner, E. Sherman, S. Soukiazian, M. Verbrugge, H. Tatara, J. Musser, P. Finamore, *J. Power Sources* 196 (2011) 3942–3948.
- [7] M. Dubarry, B.Y. Liaw, M.S. Chen, S.S. Chyan, K.C. Han, W.T. Sie, S.H. Wu, *J. Power Sources* 196 (2011) 3420–3425.
- [8] P. Liu, J. Wang, J. Hicks-Garner, E. Sherman, S. Soukiazian, M. Verbrugge, H. Tatara, J. Musser, P. Finamore, *J. Electrochem. Soc.* 157 (2010) A499–A507.
- [9] X. Han, M. Ouyang, L. Lu, J. Li, Y. Zheng, Z. Li, *J. Power Sources* 251 (2014) 38–54.
- [10] R.S. Rubino, H. Gan, E.S. Takeuchi, *J. Electrochem. Soc.* 148 (2001) A1029–A1033.
- [11] K. Maher, R. Yazami, *J. Power Sources* 247 (2014) 527–533.
- [12] A. Eddahech, O. Briat, H. Henry, J.Y. Deléage, E. Woigard, J.M. Vinassa, *Microelectron. Reliab.* 51 (2011) 1968–1971.
- [13] F. Todeschini, S. Onori, G. Rizzoni, in: 8th IFAC Symposium on Fault Detection, Supervision and Safety of Technical Processes (SAFEPROCESS), Mexico City, Mexico, 2012, pp. 456–461.
- [14] M. Dubarry, V. Svoboda, R. Hwu, B.Y. Liaw, *J. Power Sources* 165 (2007) 566–572.
- [15] G. Ning, B. Haran, B.N. Popov, *J. Power Sources* 117 (2003) 160–169.
- [16] P.L. Moss, G. Au, E.J. Plichta, J.P. Zheng, *J. Electrochem. Soc.* 157 (2010) A1–A7.
- [17] M. Dubarry, V. Svoboda, R. Hwu, B.Y. Liaw, *J. Power Sources* 174 (2007) 1121–1125.
- [18] T. Sasaki, T. Nonaka, H. Oka, C. Okuda, Y. Itou, Y. Kondo, Y. Takeuchi, Y. Ukyo, K. Tatsumi, S. Muto, *J. Electrochem. Soc.* 156 (2009) A289–A293.
- [19] M. Dubarry, C. Truchot, B.Y. Liaw, *J. Power Sources* 258 (2014) 408–419.
- [20] J. Shim, K.A. Striebel, *J. Power Sources* 122 (2003) 188–194.
- [21] U. Tröltzsch, O. Kanoun, H.-R. Tränkle, *Electrochim. Acta* 51 (2006) 1664–1672.
- [22] K. Takei, K. Kumai, Y. Kobayashi, H. Miyashiro, N. Terada, T. Iwahori, T. Tanaka, *J. Power Sources* 97–98 (2001) 697–701.
- [23] Y. Zhang, C.Y. Wang, *J. Electrochem. Soc.* 156 (2009) A527–A535.
- [24] Y. Zhang, C.Y. Wang, X. Tang, *J. Power Sources* 196 (2011) 1513–1520.
- [25] J. Shim, R. Kostecki, T. Richardson, X. Song, K.A. Striebel, *J. Power Sources* 112 (2002) 222–230.
- [26] M. Dubarry, C. Truchot, B.Y. Liaw, K. Gering, S. Sazhin, D. Jamison, C. Michelbacher, *J. Power Sources* 196 (2011) 10336–10343.
- [27] P. Gyan, P. Aubret, J. Hafsaoui, F. Sellier, S. Bourlot, S. Zinola, F. Badin, in: IFPEN (Ed.), *Les Rencontres Scientifiques D'IFP Energies Nouvelles – Int. Scient. Conf. On Hybrid and Electric Vehicles – RHEVE 2011*, 2011.
- [28] S.S. Choi, H.S. Lim, *J. Power Sources* 111 (2002) 130–136.
- [29] D. Aurbach, E. Zinigrad, H. Teller, P. Dan, *J. Electrochem. Soc.* 147 (2000) 1274–1279.
- [30] M. Dubarry, B.Y. Liaw, *J. Power Sources* 194 (2009) 541–549.
- [31] M. Dubarry, V. Svoboda, R. Hwu, B.Y. Liaw, *Electrochem. Solid State Lett.* 9 (2006) A454–A457.

- [32] S.-W. Eom, M.-K. Kim, I.-J. Kim, S.-I. Moon, Y.-K. Sun, H.-S. Kim, *J. Power Sources* 174 (2007) 954–958.
- [33] N. Omar, M.A. Monem, Y. Firouz, J. Salminen, J. Smekens, O. Hegazy, H. Gaulous, G. Mulder, P. Van den Bossche, T. Coosemans, J. Van Mierlo, *Appl. Energy* 113 (2014) 1575–1585.
- [34] S.B. Peterson, J. Apt, J.F. Whitacre, *J. Power Sources* 195 (2010) 2385–2392.
- [35] I. Bloom, S.A. Jones, E.G. Polzin, V.S. Battaglia, G.L. Henriksen, C.G. Motloch, R.B. Wright, R.G. Jungst, H.L. Case, D.H. Doughty, *J. Power Sources* 111 (2002) 152–159.
- [36] Z. Li, L. Lu, M. Ouyang, Y. Xiao, *J. Power Sources* 196 (2011) 9757–9766.
- [37] R.B. Wright, J.P. Christophersen, C.G. Motloch, J.R. Belt, C.D. Ho, V.S. Battaglia, J.A. Barnes, T.Q. Duong, R.A. Sutula, *J. Power Sources* 119–121 (2003) 865–869.
- [38] J.-W. Lee, Y.K. Anguchamy, B.N. Popov, *J. Power Sources* 162 (2006) 1395–1400.
- [39] D. Zhang, B.S. Haran, A. Durairajan, R.E. White, Y. Podrazhansky, B.N. Popov, *J. Power Sources* 91 (2000) 122–129.
- [40] J.R. Belt, C.D. Ho, T.J. Miller, M.A. Habib, T.Q. Duong, *J. Power Sources* 142 (2005) 354–360.
- [41] X.-Y. Zhou, Y.-L. Zou, G.-J. Zhao, J. Yang, *Trans. Nonferrous Metals Soc. China* 23 (2013) 3040–3045.
- [42] L. Lam, in: *Electrical Power Engineering, Electrical Engineering, Mathematics and Computer Science Faculty, University of Technology Delft*, 2011.
- [43] J.P. Christophersen, C.G. Motloch, C.D. Ho, D.F. Glenn, R.B. Wright, J.R. Belt, T.C. Murphy, T.Q. Duong, V.S. Battaglia, in: *Idaho National Engineering and Environmental Laboratory & Bechtel BWXT Idaho (LLC)*, 2002.
- [44] D. Anseán, M. González, J.C. Viera, V.M. García, C. Blanco, M. Valledor, *J. Power Sources* 239 (2013) 9–15.
- [45] M.M. Joglekar, N. Ramakrishnan, *J. Power Sources* 230 (2013) 143–147.
- [46] B. Stiaszny, J.C. Ziegler, E.E. Krauß, J.P. Schmidt, E. Ivers-Tiffée, *J. Power Sources* 251 (2014) 439–450.
- [47] S. Brown, K. Ogawa, Y. Kumeuchi, S. Enomoto, M. Uno, H. Saito, Y. Sone, D. Abraham, G. Lindbergh, *J. Power Sources* 185 (2008) 1444–1453.
- [48] J. Cannarella, C.B. Arnold, *J. Power Sources* 245 (2014) 745–751.
- [49] J. Belt, V. Utgikar, I. Bloom, *J. Power Sources* 196 (2011) 10213–10221.
- [50] S. Käbitz, J.B. Gerschler, M. Ecker, Y. Yurdagel, B. Emmertmacher, D. André, T. Mitsch, D.U. Sauer, *J. Power Sources* 239 (2013) 572–583.
- [51] M. Ecker, N. Nieto, S. Käbitz, J. Schmalstieg, H. Blanke, A. Warnecke, D.U. Sauer, *J. Power Sources* 248 (2014) 839–851.
- [52] M. Ecker, J.B. Gerschler, J. Vogel, S. Käbitz, F. Hust, P. Dechent, D.U. Sauer, *J. Power Sources* 215 (2012) 248–257.
- [53] R.B. Wright, C.G. Motloch, J.R. Belt, J.P. Christophersen, C.D. Ho, R.A. Richardson, I. Bloom, S.A. Jones, V.S. Battaglia, G.L. Henriksen, T. Unkelhaeuser, D. Ingersoll, H.L. Case, S.A. Rogers, R.A. Sutula, *J. Power Sources* 110 (2002) 445–470.
- [54] K. Amine, C.H. Chen, J. Liu, M. Hammond, A. Jansen, D. Dees, I. Bloom, D. Vissers, G. Henriksen, *J. Power Sources* 97–98 (2001) 684–687.
- [55] I. Bloom, B.W. Cole, J.J. Sohn, S.A. Jones, E.G. Polzin, V.S. Battaglia, G.L. Henriksen, C. Motloch, R. Richardson, T. Unkelhaeuser, D. Ingersoll, H.L. Case, *J. Power Sources* 101 (2001) 238–247.
- [56] R.G. Jungst, G. Nagasubramanian, H.L. Case, B.Y. Liaw, A. Urbina, T.L. Paez, D.H. Doughty, *J. Power Sources* 119–121 (2003) 870–873.
- [57] M. Safari, C. Delacourt, *J. Electrochem. Soc.* 158 (2011) A1123–A1135.
- [58] C. Delacourt, M. Safari, *J. Electrochem. Soc.* 159 (2012) A1283–A1291.
- [59] I. Bloom, S.A. Jones, V.S. Battaglia, G.L. Henriksen, J.P. Christophersen, R.B. Wright, C.D. Ho, J.R. Belt, C.G. Motloch, *J. Power Sources* 124 (2003) 538–550.
- [60] G. Sarre, P. Blanchard, M. Broussely, *J. Power Sources* 127 (2004) 65–71.
- [61] I. Bloom, L.K. Walker, J.K. Basco, D.P. Abraham, J.P. Christophersen, C.D. Ho, *J. Power Sources* 195 (2010) 877–882.
- [62] I. Bloom, B.G. Potter, C.S. Johnson, K.L. Gering, J.P. Christophersen, *J. Power Sources* 155 (2006) 415–419.
- [63] J.P. Christophersen, C.D. Hoa, C.G. Motloch, D. Howell, H.L. Hess, *J. Electrochem. Soc.* 153 (2006) A1406–A1416.
- [64] B. Lunz, Z. Yan, J.B. Gerschler, D.U. Sauer, *Energy Policy* 46 (2012) 511–519.
- [65] M.C. Smart, B.V. Ratnakumar, L.D. Whitcanack, F.J. Puglia, S. Santee, R. Gitzendanner, *Int. J. Energy Res.* 34 (2010) 116–132.
- [66] M. Klett, R. Eriksson, J. Groot, P. Svens, K. Ciosek Högstrom, R.W. Lindström, H. Berg, T. Gustafson, G. Lindbergh, K. Edström, *J. Power Sources* 257 (2014) 126–137.
- [67] D. Aurbach, B. Markovsky, Y. Talyossef, G. Salitra, H.-J. Kim, S. Choi, *J. Power Sources* 162 (2006) 780–789.
- [68] J. Schmalstieg, S. Käbitz, M. Ecker, D.U. Sauer, *J. Power Sources* 257 (2014) 325–334.
- [69] T.G. Zavalis, M. Klett, M.H. Kjell, M. Behm, R.W. Lindström, G. Lindbergh, *Electrochim. Acta* 110 (2013) 335–348.
- [70] S. Muto, Y. Sasano, K. Tatsumi, T. Sasaki, K. Horibuchi, Y. Takeuchi, Y. Ukyo, *J. Electrochem. Soc.* 156 (2009) A371–A377.
- [71] M.J. Plancha, C.M. Rangel, B. Rodrigues, F. Azevedo, *Ciência Tecnol. Mater.* 23 (2011) 59–66.
- [72] K. Amine, J. Liu, I. Belharouak, *Electrochem. Commun.* 7 (2005) 669–673.
- [73] D. Aurbach, B. Markovsky, A. Rodkin, E. Levi, Y.S. Cohen, H.J. Kim, M. Schmidt, *Electrochim. Acta* 47 (2002) 4291–4306.
- [74] I. Bloom, J.P. Christophersen, D.P. Abraham, K.L. Gering, *J. Power Sources* 157 (2006) 537–542.
- [75] X.V. Zhang, P.N. Ross, R. Kostecki, F. Kong, S. Sloop, J.B. Kerr, K. Striebel, E.J. Cairns, F. McLarnon, *J. Electrochem. Soc.* 148 (2001) A463–A470.
- [76] S. Bourlot, P. Blanchard, S. Robert, *J. Power Sources* 196 (2011) 6841–6846.
- [77] I. Bloom, J. Christophersen, K. Gering, *J. Power Sources* 139 (2005) 304–313.
- [78] S. Onori, P. Spagnol, V. Marano, Y. Guezennec, G. Rizzoni, *J. Power Electron.* 4 (2012) 302–319.
- [79] J. Groot, in: *Division of Electric Power Engineering, Department of Energy and Environment, Chalmers University of Technology Göteborg, Sweden*, 2012.
- [80] T.M. Bandhauer, S. Garimella, T.F. Fuller, *J. Power Sources* 247 (2014) 618–628.
- [81] E.V. Thomas, I. Bloom, J.P. Christophersen, V.S. Battaglia, *J. Power Sources* 184 (2008) 312–317.
- [82] K.J. Chung, C.C. Hsiao, in: *International Symposium on Computer, Consumer and Control (IS3C)*, Taichung, Taiwan, 2012.
- [83] E.V. Thomas, I. Bloom, J.P. Christophersen, V.S. Battaglia, *J. Power Sources* 206 (2012) 378–382.
- [84] E. Sarasketa-Zabala, I. Laresgoiti, I. Alava, M. Rivas, I. Villarreal, F. Blanco, in: *EV527, Barcelona, Spain*, 2013.
- [85] H. Joachin, T.D. Kaun, K. Zaghib, J. Prakash, *J. Electrochem. Soc.* 156 (2009) A401–A406.
- [86] B. Scrosati, J. Garche, *J. Power Sources* 195 (2010) 2419–2430.
- [87] A.K. Padhi, K.S. Nanjundaswamy, J.B. Goodenough, *J. Electrochem. Soc.* 144 (1997) 1188–1194.
- [88] A. Yamada, S.C. Chung, K. Hinokuma, *J. Electrochem. Soc.* 148 (2001) A224–A229.
- [89] N. Ravet, Y. Chouinard, J.F. Magnan, S. Besner, M. Gauthier, M. Armand, *J. Power Sources* 97–98 (2001) 503–507.
- [90] H. Huang, S.C. Yin, L.F. Nazar, *Electrochem. Solid State Lett.* 4 (2001) A170–A172.
- [91] Z. Chen, J.R. Dahn, *J. Electrochem. Soc.* 149 (2002) A1184–A1189.
- [92] S.Y. Chung, J.T. Bloking, Y.M. Chiang, *Nat. Mater.* 1 (2002) 123–128.
- [93] S. Franger, F.L. Cras, C. Bourbon, H. Rouault, *J. Electrochem. Soc.* 151 (2004) A1024–A1027.
- [94] E. Sarasketa-Zabala, I. Gandiaga, L.M. Rodriguez-Martinez, I. Villarreal, *J. Power Sources* 272 (2014) 45–57.
- [95] M. Kassem, J. Bernard, R. Revel, S. Pélissier, F. Duclaud, C. Delacourt, *J. Power Sources* 208 (2012) 296–305.
- [96] R. Spotnitz, *J. Power Sources* 113 (2003) 72–80.
- [97] R. Deshpande, Y. Cheng, M.W. Verbrugge, A. Timmons, *J. Electrochem. Soc.* 158 (2011) A718–A724.
- [98] J.R. Dahn, *Phys. Rev. B* 44 (1991) 9170–9177.
- [99] E. Scott, J. Brown, C. Schmidt, W. Howard, in: *208th ECS Meeting Los Angeles, California*, 2005.
- [100] M. Dubarry, C. Truchot, B.Y. Liaw, *J. Power Sources* 219 (2012) 204–216.
- [101] R. Yazami, Y.F. Reynier, *Electrochim. Acta* 47 (2002) 1217–1223.
- [102] H. Wenzl, A. Haubrock, H.P. Beck, *Z. Phys. Chem.* 227 (2013) 57–71.
- [103] M. Lepiorz, W. Weydanz, D. Most, A. Jossen, in: *5th Advanced Battery Power Aachen, Germany*, 2013.